ACS APPLIED MATERIALS & INTERFACES

Research Article

www.acsami.org

Enhancing the Electromagnetic Performance of Co through the Phase-Controlled Synthesis of Hexagonal and Cubic Co Nanocrystals Grown on Graphene

Guohua Pan,[†] Jia Zhu,[†] Shulan Ma,*[,†] Genban Sun,*[,†,‡] and Xiaojing Yang[†]

[†]Beijing Key Laboratory of Energy Conversion and Storage Materials and College of Chemistry, Beijing Normal University, Beijing 100875, China

[‡]Department of Materials Physics and Chemistry, University of Science and Technology Beijing, Beijing 100083, China

Supporting Information

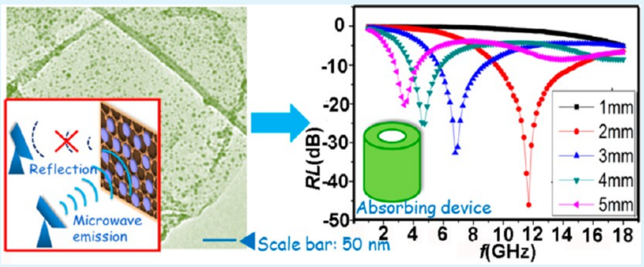

ABSTRACT: Cobalt is a promising soft metallic magnetic material used for important applications in the field of absorbing stealth technology, especially for absorbing centimeter waves. However, it frequently presents a weak dielectric property because of its instability, aggregation, and crystallographic form. A method for enhancing the electromagnetic property of metal Co via phase-controlled synthesis of Co nanostructures grown on graphene (GN) networks has been developed. Hexagonal close-packed cobalt (α-Co) nanocrystals and face-centered cubic cobalt (β-Co) nanospheres with uniform size and high dispersion have been successfully assembled on GN nanosheets via a facile one-step solution-phase strategy under different reaction conditions in which the exfoliated graphite oxide (graphene oxide, GO) nanosheets were reduced along with the formation of Co nanocrystals. The as-synthesized Co/GN nanocomposites showed excellent microwave absorbability in comparison with the corresponding Co nanocrystals or GN, especially for the nanocomposites of GN and α-Co nanocrystals (the reflection loss is −47.5 dB at 11.9 GHz), which was probably because of the special electrical properties of the cross-linked GN nanosheets and the perfect electromagnetic match in their microstructure as well as the small particle size of Co nanocrystals. The approach is convenient and effective. Some magnetic metal or alloy materials can also be prepared via this route because of its versatility.

KEYWORDS: *cobalt, graphene, microwave absorbability, nanostructures, electromagnetic performance*

1. INTRODUCTION

In recent years, the influence of electromagnetic (EM) radiation on health has received increasing attention with the development of technology. Considerable theoretical and experimental investigations have been focused on designing and fabricating effective electromagnetic wave absorption materials with promising applications in electronic devices for commercial, industrial, and military affairs. Because of the tremendous progress in absorbing stealth technology, EM-absorbing materials with a thin thickness, light quality, high reflection loss, and broad band are required. According to these requirements, the crucial factors that influence the performance of the absorbing materials are their complex permittivity and permeability. Therefore, magnetic and conductive nanomaterials continue to play a leading role in the investigation and application of microwave absorbers. It is well-known that small sized metal cobalt nanocrystals have advantages for high-EM performance because they are typical soft metallic magnetic materials and show large magnetic anisotropy.[1−5] However, Co nanoclusters are readily agglomerated and oxidized when exposed to the air, which may result in antiferromagnetic cobalt oxide and decreased dielectric properties. Therefore, dispersing and preserving the natural structure of cobalt nanoparticles with oxygen-impermeable guest materials are necessary prerequisites for their potential use in microwave-absorbance applications. To meet these demands, significant progress has been made to design materials that can protect the cobalt nanomaterials, including the utilization of different structured carbon materials,[6−9] various polymers,[10−14] zeolite-structured materials,[15−17] and so on. GN nanosheets are perfect substrates to support the active nanoparticles for use in applications as functional materials because of their excellent electrical properties, large surface area, light weight, flexibility, and corrosion resistance.[18,19] Since graphene was successfully reported by Geim and co-workers in 2004,[20] many important research results have been reported on the preparation of magnetic graphene nanocomposites including nanoparticles of Mn_3O_4,[18] MoS_2,[21] Fe_3O_4,[22−27] FePt,[28] $Ni(OH)_2$,[29] Ge,[19] and so on. However, to the best of our knowledge, face-centered cubic Co nanocrystals growing on graphene have rarely been

Received: September 21, 2013
Accepted: November 18, 2013
Published: November 18, 2013

dx.doi.org/10.1021/am404117v | *ACS Appl. Mater. Interfaces* 2013, 5, 12716−12724

studied apart from several reports on hexagonal close-packed cobalt.[30−34] Magnetic Co nanostructures with different phases and sizes grown on graphene nanosheets have been of great interest for EM-wave-absorption applications because of the excellent magnetic property of Co nanostructures. Moreover, for EM-wave-absorbing materials, GN nanosheets can acts as a crucial component because of their advantages described above, which may make the nanocomposites more attractive than polymer matrix nanocomposites. In addition, compared with other carbon composites such as fullerene, carbon black, and carbon nanotubes, GN nanosheets can also supply good dispersion and protection for magnetic metal nanocrystals and provide a high monodirectional electrical conductivity of the overall microwave-absorbing device, which is favorable for obtaining an excellent dielectric property. Generally, most of the present absorbing materials often show the EM-wave-absorption region at high frequency (12−18 GHz). It is still a challenge to prepare microwave absorbers that possess strong absorption at the frequency of the low (1−6 GHz) or middle (6−12 GHz) band. Therefore, it is significant to study materials with an absorbing property at a low or middle frequency in the range of 1−18 GHz and to determine clearly the correlation between the microstructure and electromagnetic performance.

As is known, metallic Co has three crystal structures (i.e., the hexagonal close-packed (hcp) α-phase,[35−37] the face-centered cubic (fcc) β-phase,[38,39] and a primitive (or pseudo-) cubic ε-phase).[40−44] Both hcp- and fcc-Co phases are more stable than ε-phase Co. Although the only crystalline structure difference is the stacking sequence of the atomic plane in the (111) direction, Co nanocrystals with different crystal structures may show distinguishing magnetic properties.[45] Therefore, it is urgent to design small magnetic Co nanocrystals with different crystal structures that are tightly assembled on GN with excellent electrical properties for use as stable, effective, light weight, and environmentally friendly microwave absorbers. Very recently, a facile one-step solution-phase route for assembling Ni nanocrystals with uniform size and high dispersion decorated on GN nanosheets under different reaction conditions was proposed by our research group.[46] It may be a more promising strategy to synthesize cobalt nanoparticles because the method is low cost, versatility, and potential for large-scale production. Herein, we propose and realize an effective strategy for enhancing the electromagnetic performance of cobalt through the phase-controlled synthesis of hexagonal and cubic cobalt nanocrystals tightly assembled on GN nanosheets. The Co/GN nanocomposites are produced by a facile one-step solution-phase method, which shows much improved EM-wave-absorption properties in comparison with pristine Co nanostructures or GN nanosheets when used as an absorbing device for microwave absorbers.

2. EXPERIMENTAL SECTION

As illustrated in Figure 1, the synthesis route for Co/GN nanocomposites and their application are schematically presented. Specific experimental details are as follows.

2.1. Preparation of Graphene Oxide. GO was synthesized from natural graphite by the modified Hummers' method, which was used as the raw material for the fabrication of Co/graphene hybrid nanomaterials.

2.2. Preparation of α-Co/GN Nanocomposites. In the first step, 40 mg of GO was added into 40 mL of 2-pyrrolidone, and after sonication for 2 h the mixture turned to a homogeneous brown solution. In the second step, 2 mmol Cobalt(II) acetylacetonate and 2 g of octadecylamine were added into the above-mentioned solution, and then the solution was heated at 120 °C and maintained at this temperature for 30 min to form the Co complex (the intermediate compound) as the precursor of the Co nanoparticles. In the third step, the temperature of the solution was increased to 245 °C, which is the boiling temperature of 2-pyrrolidone, and maintained for 2 h. During the first three steps of the reaction, the reaction system was magnetically stirred under a flow of argon gas, and the color of the solution turned from red to brown. In the fourth step, when the reaction was finished, 20 mL of ethanol was injected into the solution to make the temperature drop quickly. In the last step, the final product was separated by centrifugation, washed alternately several times with *n*-hexane and acetone, and dried at 40 °C under vacuum.

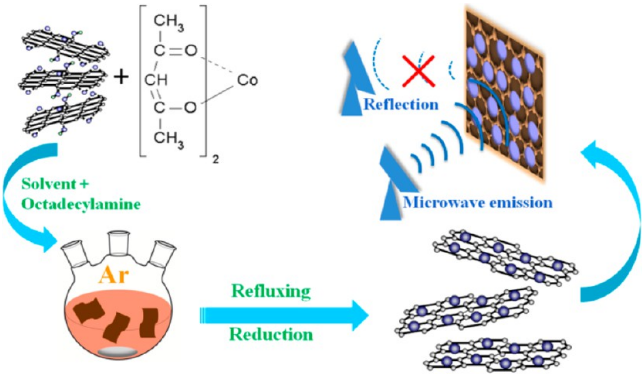

Figure 1. Schematic illustration of the Co/GN nanocomposites formation route and their application.

2.3. Preparation of β-Co/GN Nanocomposites. Similar to the synthesis of α-Co/GN composites, we employed oleylamine instead of 2-pyrrolidone as the solvent, whose boiling temperature is about 350 °C. As a result, the temperature was maintained at 290 °C for 2 h in the third step, obtaining cauliflower-like β-Co/GN nanocomposites. The separation and washing method were the same as that in the preparation of α-Co/GN composites.

2.4. Characterization. The structures of the resulting samples were analyzed by X-ray powder diffraction (XRD) employing a Phillips X'pert Pro MPD diffractometer (Cu Kα, λ = 1.54056 Å). The morphology, size, and details of the as-synthesized samples were investigated by employing a field-emission scanning electron microscope (FESEM, acceleration voltage of 5 kV, S-4800, Hitachi) and a high-resolution transmission electron microscope (HRTEM, an acceleration voltage of 200 kV, JEM-2010, JEOL). Fourier-transform infrared (FT-IR) spectra of the samples were recorded on a Nicolet-380 Fourier-transform infrared spectrometer using the KBr method in the range of 480−4000 cm^{-1}. Raman spectra were taken from 1200 to 1800 cm^{-1} on a microscopic confocal Raman spectrometer (LabRAMAramis, Horiba JobinYivon) using a 633 nm He−Ne laser. X-ray photoelectron spectroscopy (XPS) was recorded on an ESCALAB 250Xi spectrometer (Thermo Fisher) to characterize the surface composition. These products were uniformly blended with paraffin matrix with a mass ratio of 3:2 (60 wt %), and the microwave absorbing devices were prepared with a cylinder shape (Φ_{outer} = 7.00 mm and Φ_{inner} = 3.04 mm) for the characterization of their EM parameters in the 1.0−18.0 GHz band by employing a vector network analyzer (HP-E8362B, Agilent).

3. RESULTS AND DISCUSSION

As shown in Figure 1, with the presence of a high-boiling-point solvent and a reducing agent, the pyrolysis reaction of cobalt(II) acetylacetonate with a long-chain organic compound generally generates monodisperse Co nanocrystals. Moreover, the critical factor to prepare monodisperse nanocrystals is to keep the reaction solution at 120 °C for at least half of an hour before it is heated to reflux at 245 °C in 2-pyrrolidone or at 290 °C in oleylamine. However, if the reaction solution was directly heated to the boiling point from room temperature, then cobalt nanocrystals with a wide size distribution often occurred, which means that their nucleation and growth are a slow process. In the reaction system, octadecylamine is important for the formation of Co/GN, which acts as a surfactant and reductant. The final reaction temperature is another key factor in this system, which mainly affects the phase and size of the Co nanocrystals. Higher reaction temperatures can generate larger nanoparticles and can be more favorable to form a cubic phase. Because of the difference in the phase and size of Co nanoparticles, β-Co nanoparticles easily self-assembled into the microspheres as a result of their high surface energy and magnetic interactions. The results are similar to our previous reports.[46] In the process of this reaction illustrated in Figure 1, GO nanosheets with negative charge possess a strong capability to attract the dissolved Co^{2+} ions through electrostatic interactions and the actions of bonding because some functional groups, such as −OH and −COOH, were first suspended in the solvent. Subsequently, the formation of Co nanocrystals, the reduction of GO nanosheets, and the assembly of Co nanocrystals on GN nanosheets occurred simultaneously via the effective in situ route in the presence of octadecylamine. It is worth mentioning that there were no additional molecules to bridge the Co nanocrystals and GN matrixes. However, Co nanocrystals can be firmly anchored on the GN sheets because of the electrostatic interactions, the actions of bonding of the remaining group, and the flexibility of GN.

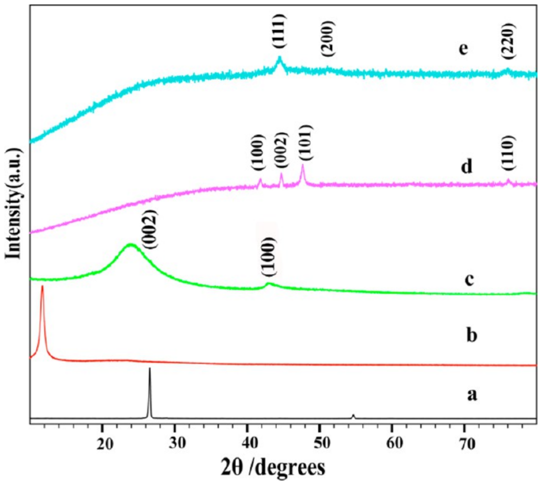

Figure 2. XRD patterns of (a) graphite, (b) GO, (c) GN, (d) as-prepared α-Co/GN, and (e) β-Co/GN nanocomposites.

XRD patterns for the as-obtained nanocomposites of α-Co and β-Co nanostructures with GN nanosheets in comparison with original graphite, graphite oxide, and graphene are illustrated in Figure 2. For graphite, the peaks at 26.5° in Figure 2a was attributed to the characteristic (002) diffraction peak of the lattice plane (002), with d spacing of ca. 0.34 nm. As shown in Figure 2b, when the graphite was oxidized, the diffraction peak shifted to the lower angle at about 10.9° with a larger d spacing of 0.76 nm, and the two weak peaks at about 23° and 42° were not found, which confirmed that the oxidation of graphite was effective. From Figure 2c, two weak and broad diffraction peaks appeared at 23.5° and 41.9°, which were identified as the lattice planes of (002) and (100) for GN, respectively. These results confirmed the existence of an amorphous carbon structure, indicating that GO was well-reduced and the stacking of graphene was substantially disordered. As illustrated in Figure 2d, four peaks observed at a 2θ of 41.59, 44.26, 47.39, and 75.89° well match the JCPDS card no. 89-4308, which could be indexed to the hexagonal close-packed (hcp) structure α-phase of cobalt with lattice parameters of a = b = 2.505 nm and c=4.089 nm, without impurity phase observed. In this reaction system, the reaction temperature affect on the phase of the Co nanoparticles, so β-Co/GN nanocomposites can be obtained by varying the reaction temperature. The XRD pattern of the as-prepared β-Co/GN nanocomposites shown in Figure 2e matches the face-centered cubic structure β-phase Co with lattice parameters of a = b = c = 3.544 nm (JCPDS card no. 89-4307). From Figure 2d,e, regardless of whether GO was present, we also confirmed that pure α-Co and β-Co nanostructures with the same morphologies can be produced via the thermal decomposition of an organometallic precursor by controlling the reaction temperature or by varying the solvent. The weak peak at 23.5° for both of the nanocomposites is attributed to GN coreduced from GO nanosheets accompanied by the generation of Co nanocrystals.

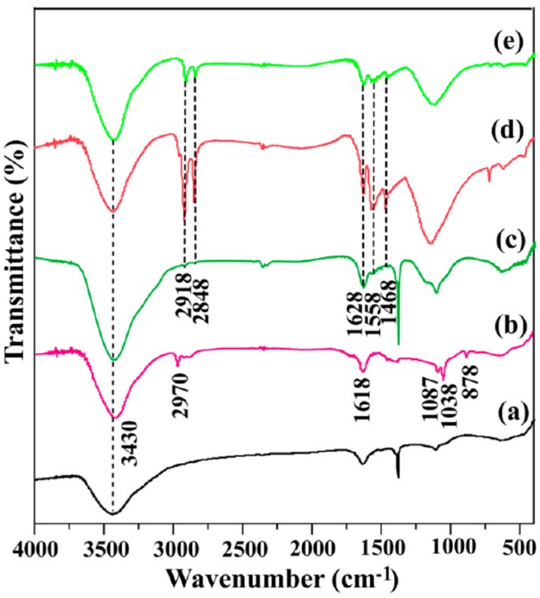

Figure 3. FT-IR spectra of (a) graphite, (b) GO, (c) GN, (d) as-prepared α-Co/GN, and (e) β-Co/GN nanocomposites.

FT-IR spectroscopy was further used to examine the degree of GO reduction, which is shown in Figure 3. For graphite oxide, the peaks at 3430 and 1618 cm^{-1} can be identified as the O−H stretching vibration of intercalated water and the skeletal vibrations of unoxidized graphitic regions or the stretching deformation vibration of intercalated water, respectively. The bands at 2970 and 1038 cm^{-1} are the alkyl C−H stretching vibration and C−O stretching vibrations, respectively. In the two as-prepared Co/GN nanocomposites, these oxygen-containing functional groups are distinctly reduced. Compared to GO, the peaks of some oxygen-containing functional groups vanished, and a new bands at 2918, 2848, and 1558 cm^{-1} emerged, which are the alkyl C−H stretching vibration and the aromatic skeletal C=C stretching vibration of GN nanosheets.[47] Moreover, the absorption of 1628 cm^{-1} remains, which is similar to that of natural graphite (Figure 3a), demonstrating that GN with a high purity may be obtained. In view of the above-mentioned data, we conclude that the GO in the Co/GN nanocomposites is completely reduced. In addition, the peak positions in patterns c, d, and e are close despite having very small shifts. This indicates that the functional groups are similar in the two as-prepared materials and graphene.

The Raman spectra of graphite, GO, GN, as-prepared α-Co/GN, and β-Co/GN nanocomposites are illustrated in Figure 4, which further support the reduction of GO during the synthesis of Co/GN nanocomposites. Significant structural variations of the carbon framework were accompanied by the chemical process of going from graphite to graphite oxide and subsequently toward GN. The variations were also reflected in their Raman spectra. However, there are two fundamental variations observed in the Raman spectra of the samples. One of these variations is at 1578 and 1332 cm^{-1} for graphite (curve a), at 1603 and 1343 cm^{-1} for GO (curve b), at 1579 and 1327 cm^{-1} for GN (curve c), at 1595 and 1330 cm^{-1} for α-Co/GN (curve d), and at 1596 and 1327 cm^{-1} for β-Co/GN nanocomposites, which are attributed to the G and D bands, respectively. The G band corresponds to the in-plane vibration of sp^2 carbon atoms in a 2D hexagonal lattice, whereas the D band corresponds to the vibrations of sp^3 carbon atoms of disordered graphite. The typical characteristic for the reduction of graphite oxide is that the G band shifts to a lower number.[27] As shown in Figure 4, the G band of Co/GN nanocomposites shifts to 1595 and 1596 cm^{-1} compared to 1603 cm^{-1} of GO, indicating the reduction of the latter. The other variation is in the ordered and disordered crystal structures of carbon that can be evaluated by employing the intensity ratio of the D and G bands (I_D/I_G). From Figure 4a–e, we calculated the value of I_D/I_G as 0.30:1 for graphite, 0.96:1 for graphite oxide, 1.38:1 for graphene, 1.15:1 for α-Co/GN, and 1.24:1 for β-Co/GN, respectively. The I_D/I_G ratio increases when GO is reduced. The variations in the value of I_D/I_G confirm that the reduction of graphite oxide can result in small-sized GN nanosheets and that a large-scale of sp^2 carbon atoms appeared in the structures.[27] The conclusions from the Raman spectra and FT-IR spectra analysis are in accord with the above XRD results and reveal that Co/GN nanocomposites could be obtained via this versatile strategy. (The conclusions from the Raman spectra and FT-IR spectra analysis are well in agreement with the XRD data and reveal that the Co/GN nanocomposites could be achieved by the method used here.)

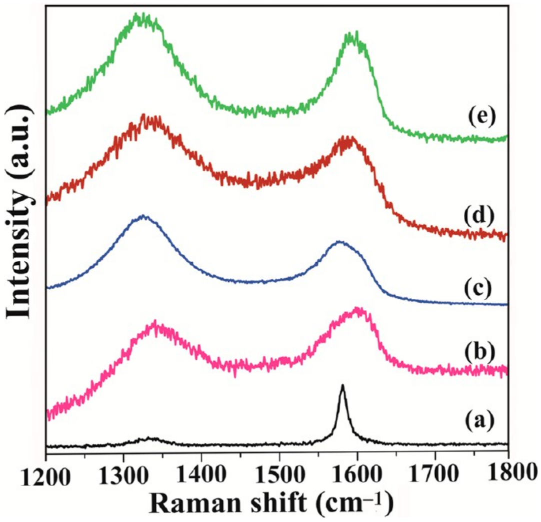

Figure 4. Raman spectroscopy of (a) graphite, (b) GO, (c) GN, (d) as-prepared α-Co/GN, and (e) β-Co/GN nanocomposites.

The surface composition of GO and Co/GN nanocomposites was further confirmed by XPS measurements. In the XPS spectra (Figure 5a), the main peaks observed in the survey scans of the two nanocomposites are C 1s, O 1s, and Co 2p peaks centered at ca. 285, 530, and 778–800 eV, respectively. For the nanocomposites, the C 1s peak intensity increases and becomes much higher than the O 1s peak. This can be interpreted by the existence of the GN matrix. The C 1s XPS spectra for GO in Figure 5b could be identified into C entities with oxygen functionalities (i.e., C–C (sp^2 carbon, C1), C–O (C2), and C=O (C3) bonds) with a binding energy of about 284.7, 286.8, and 288.8 eV, respectively. As shown in Figure 5c,d, the C2 peaks located at 286.0 eV and C3 peaks located at 287.7 eV became significantly weaker, which was accompanied by the formation of cobalt nanoparticles. In addition, the C/O ratio in the two Co/GN nanocomposites calculated from Figure 5b–d increase in comparison with that of GO, which is 0.8, 2.0, and 5.0 for the C/O ratio of GO, α-Co/GN, and β-Co/GN, respectively. On the basis of the XPS analysis, we conclude that a majority of oxygen-containing functional groups, such as –OH and –COOH, in the GO nanosheets were efficiently reduced. In Figure 5e,f, the peaks located at ca. 778 and 800 eV are assigned to the binding energy of Co 2p$_{3/2}$ and 2p$_{1/2}$, Figure 5e,f also shows the main peak at 778.03 eV for α-Co/GN and β-Co/GN, which can be attributed to metallic Co and reveals that zero-valent Co is obtained after reduction from Co(II).[3,48] The peaks at 781.20 and 786.30 eV (the satellite peak) for the two nanocomposites can be indexed to the Co(II) oxidation state. This result implies the possible coexistence of metallic Co and Co^{2+} in the Co/GN nanocomposites.

Representative transmission electron microscopy (TEM) images of the as-synthesized α-Co/GN nanocomposites with increasing magnification are shown in panels a and b of Figure 6, respectively. In Figure 6a,b, large-scale hexagonal close-packed cobalt (α-Co) nanocrystals with relatively uniform size were obtained. Almost no agglomeration was observed, and each piece of the sample shows the same structure. Figure 6a clearly shows that large-scale Co nanocrystals were successfully fabricated on the 2D GN nanosheets and that the edges of the GN nanosheets and Co nanocrystals can be clearly identified. As shown in Figure 6b, Co nanocrystals are orderly and evenly adhered to GN nanosheets, indicating that GN can well-disperse Co nanocrystals. Moreover, from Figure 6a–c, there are no separate Co nanoparticles and GN sheet substrates, indicating that the nanocomposites can be achieved by the one-pot method, which further demonstrated that all of the Co nanocrystals have grown on the GN nanosheets. Figure 6c,d presents the high-resolution TEM images of the α-Co/GN nanocomposites. From Figure 6c, we can clearly observe that the α-Co nanocrystals have an average diameter of around 3 nm. The HRTEM images and the SAED pattern shown in Figure 6d indicate that the size of the Co nanocrystal spreading over the GN surface is about 4 nm and the measured *d* spacing of the Co nanocrystals is 0.19 nm, corresponding to the (101) lattice plane, which is consistent with the above XRD data. The considerably sharp ring-like features including the diffraction lattice of the corresponding SAED pattern (the inset of Figure

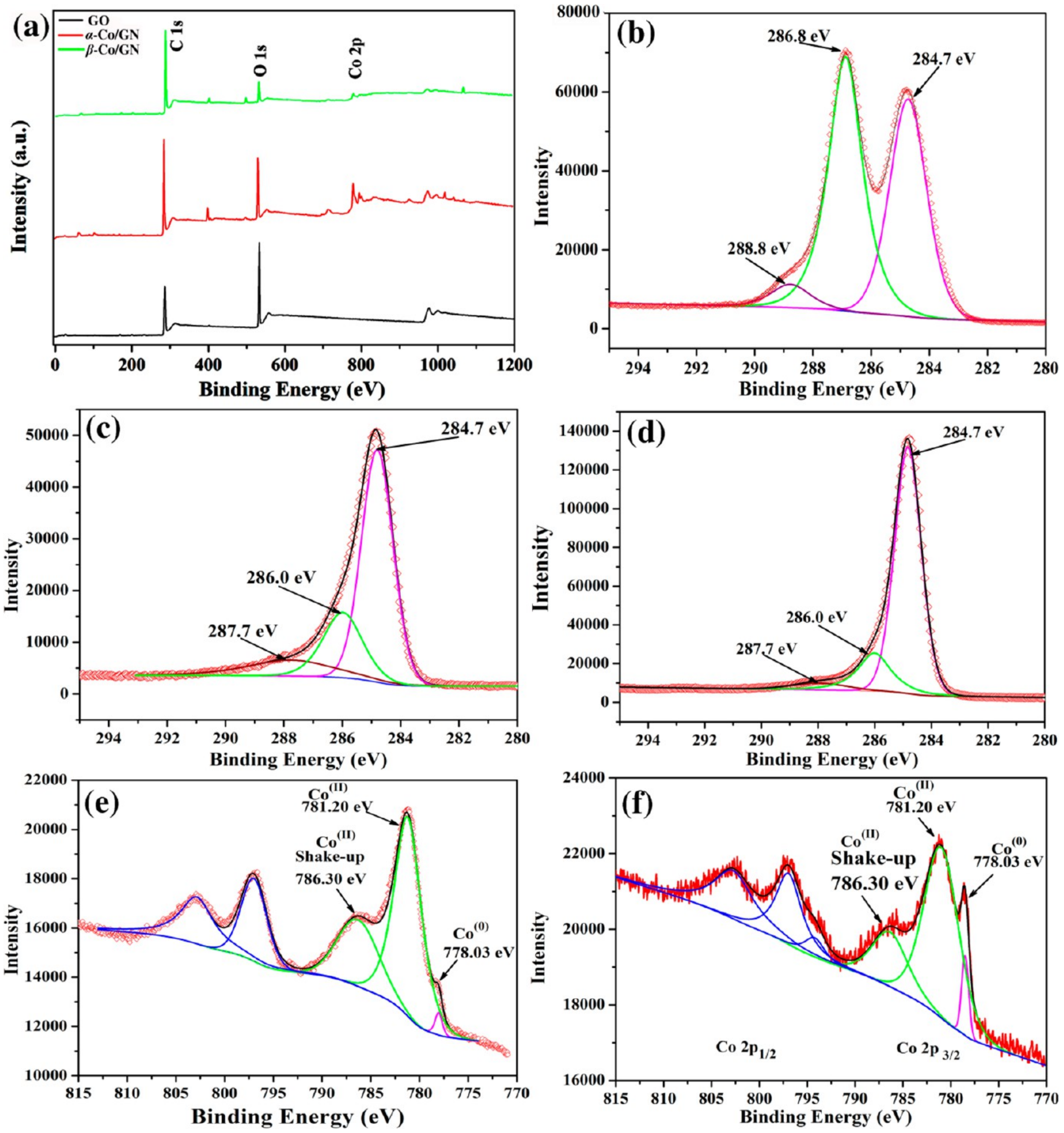

Figure 5. (a) Survey scans for XPS spectra of GO (black), α-Co/GN(red), and β-Co/GN(green) nanocomposites. C 1s peaks of (b) GO, (c) α-Co/GN, and (d) β-Co/GN nanocomposites. Co 2p peaks of (e) α-Co/GN and (f) β-Co/GN nanocomposites.

6d) indicate the polycrystalline nature of the as-obtained sample with clear (100), (002), and (101) diffractions and the typical diffraction lattice of GN sheets, which confirmed that they were well-crystallized.

As shown in Figures 7 and S1, when we changed the second heating temperature from 245 to 290 °C using oleylamine as the solvent instead of 2-pyrrolidone, face-centered cubic cobalt (β-Co) nanospheres/GN nanocomposites can be achieved on a large scale. Figure S1 clearly indicates that the nanocomposites are composed of numerous spherical microstructures with typical diameters in the narrow range of 250−350 nm wrapped by GN nanosheet matrixes. The inset of Figure S1 also clearly shows that β-Co nanospheres are completely covered by GN nanosheets. Figure 7a,b demonstrates that GN nanosheets are decorated randomly by β-Co nanospheres with a highly uniform shape and that the average diameter is ca. 300 nm, which agrees with the results in Figure S1. From Figure 7b, although it is difficult to distinguish GN sheets on the surfaces of Co nanospheres because the monolayer carbon sheets are extremely thin, we can still identify the transparent graphene sheets from the wrinkles and the vignetting of the TEM image on the surface of the Co nanospheres (see the arrow in Figure 7b), which confirmed the formation of the β-Co/GN nanocomposite networks. Figure 7c presents the high-magnification TEM images of a β-Co nansphere grown on the GN nanosheets (the arrow). As indicated in Figure 7c, cauliflower-like β-Co nanospheres are deeply and firmly embedded into the GN sheets with a tight conjugation of their edges even after ultrasonication for TEM characterization. Figure 7c also clearly shows a typical β-Co submicrometer sphere with a diameter of ca. 270 nm; the sphere is composed of β-Co nanocrystals with diameters ranging from 20 to 40 nm. The 2D lattice fringe image throughout the entire face-centered cubic Co nanospheres formed on GN nanosheets is shown in the HRTEM image (Figure 7d). The lattice fringes with a spacing of 0.176 nm may correspond to the (200) plane of face-centered cubic cobalt, which is consistent with the (200) diffraction point in the SAED analysis (the arrow in the inset of Figure 7d). The SAED pattern also clearly shows a typical diffraction lattice of GN sheets and face-centered cubic crystal

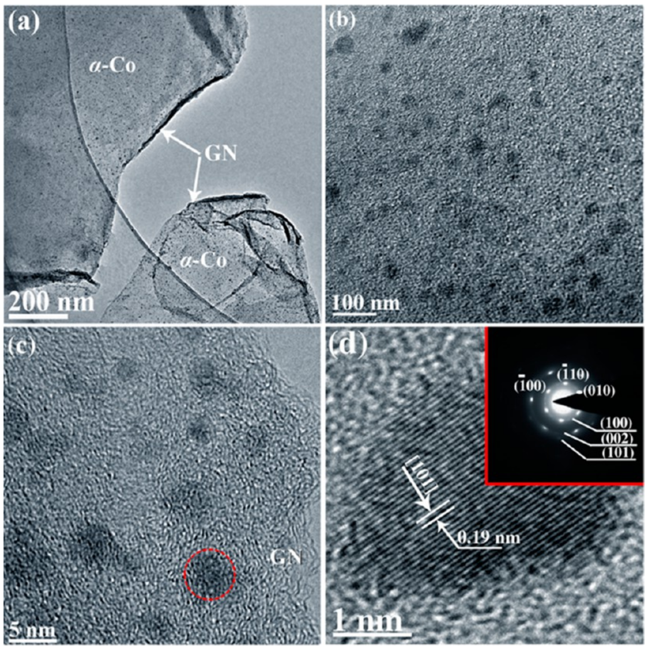

Figure 6. (a, b) TEM and (c, d) HRTEM images of α-Co/GN nanocomposites. The inset of panel d is the SAED pattern.

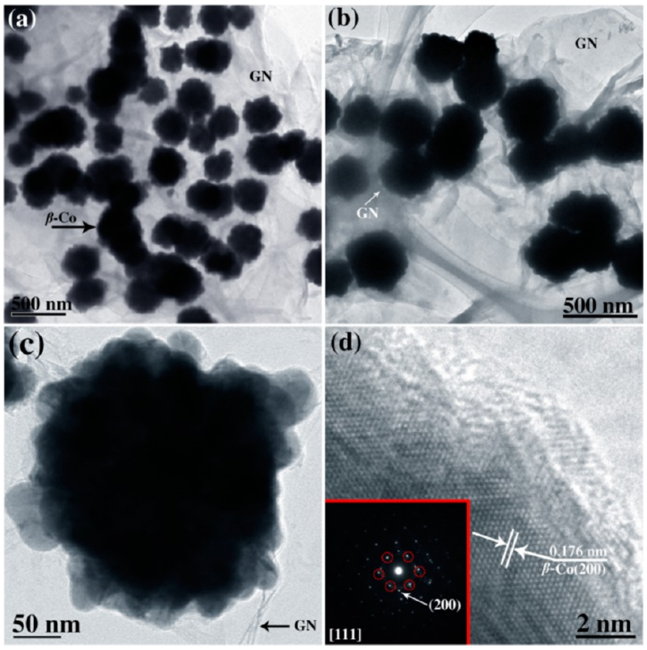

Figure 7. (a, b) TEM and (c, d) HRTEM images of β-Co/GN nanocomposites. The inset of panel d is the SAED pattern.

structure, which confirmed that they have a single-crystalline structure.

To compare and evaluate their microwave absorption properties, GN, α-Co nanocrystals, β-Co nanospheres, and their GN nanocomposites were uniformly mixed in a paraffin matrix (60 wt %), which is transparent to electromagnetic waves, and assembled into a microwave-absorption device with an outer diameter of 7.00 mm and an inner diameter of 3.04 mm, and the devices were measured in the range of 1−18 GHz by an Agilent E8362B vector network analyzer. The microwave absorption properties of the as-prepared products can be evaluated by the reflection loss (RL) values, which may be calculated by employing the permeability and permittivity at a known frequency and layer thickness on the basis of the theory for microwave transmission, which is summarized in the following equations[49−54]

$$Z_{\text{in}} = Z_0\sqrt{\mu_r/\varepsilon_r}\,\tanh[j(2\pi fd/c)\sqrt{\mu_r\varepsilon_r}] \tag{1}$$

$$\text{RL (dB)} = 20\log|(Z_{\text{in}} - Z_0)/(Z_{\text{in}} + Z_0)| \tag{2}$$

where f, d, c, Z_0, and Z_{in} are the microwave frequency, thickness of the absorber, light velocity, air impedance, and input impedance of the absorber, respectively. The results are shown in Figure 8. As illustrated in Figure 8a, the two Co/GN nanocomposites presents much stronger microwave-absorption performance than the pure metal nanostructures and the GN nanosheets. For example, when the thickness is 2 mm, for α-Co nanocrystals, there is one peak at 6.0 GHz with the minimum RL of −2.5 dB; for GN nanosheets, there is almost no electromagnetic wave-absorption peak because of the high real part of their permittivity, whereas for α-Co/GN nanocomposites, the strongest EM-wave absorption with an RL value of −47.5 dB appeared at 11.9 GHz. Compared with other nanocrystals/graphene composites, the microwave absorption of α-Co/GN with a thickness of 2 mm is superior to those in the previous reports: GN−Fe_3O_4 nanohybrids with an average diameter of 25 nm (−40.36 dB at 7.0 GHz, 5 mm),[55] GN-Fe_3O_4 nanoparticles with sizes of about 30 nm (−26.4 dB at 5.3 GHz, 4.0 mm),[56] monodispersed GN−hematite nanocomposites around 120 nm in diameter (−35.8 dB at 6.1 GHz, 5 mm),[57] and our previous report.[46] For β-Co nanospheres, one

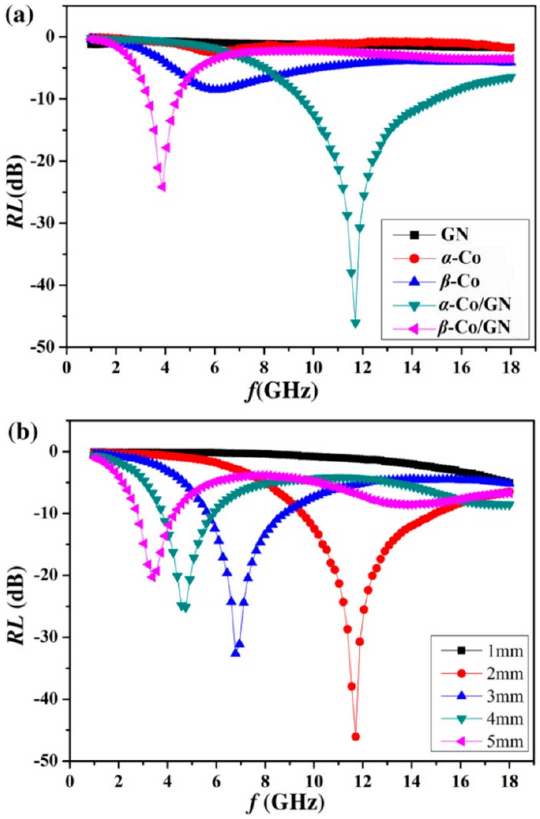

Figure 8. (a) Comparison of microwave reflection losses of the five as-obtained samples with a thickness of 2 mm. (b) Microwave reflection losses of α-Co/GN nanocomposites with different thicknesses.

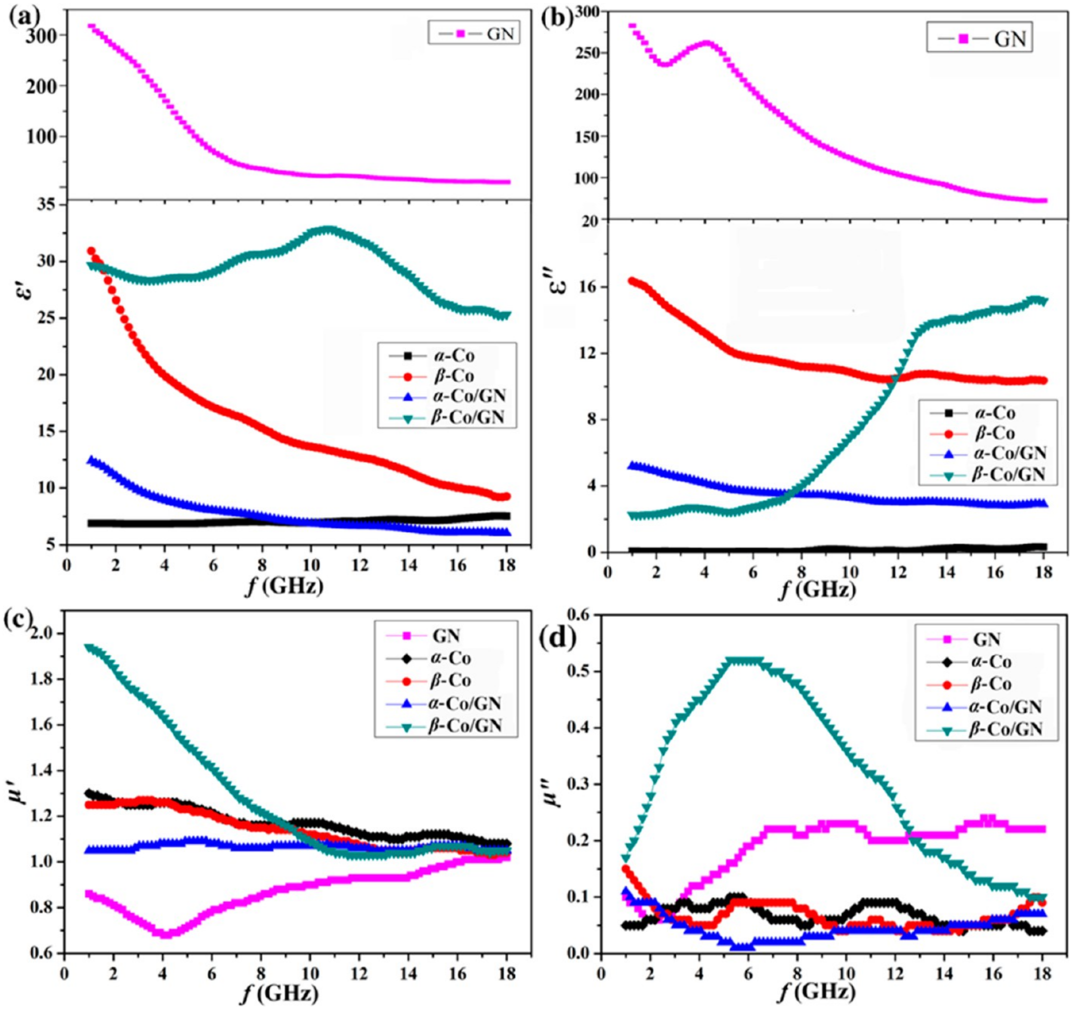

Figure 9. Frequency dependence of the (a) real and (b) imaginary parts of complex permittivity and the (c) real and (d) imaginary parts of complex permeability for the five as-prepared samples.

peak (5.9 GHz, −8.5 dB) was observed, whereas for β-Co nanospheres/GN nanocomposites, a narrow and strong peak (3.8 GHz, −24.1 dB) was observed. The absorbtion data demonstrate that the EM performance of cobalt nanostructures can be significantly enhanced through the phase-controlled synthesis of hexagonal and cubic cobalt nanocrystals grown on graphene nanosheets, which makes them a promising microwave-absorption material for use in effective shielding devices. The thickness of the absorber, as one of critical factors, will influence the RL value and the frequency of maximum absorption. Hence, we fabricated α-Co/GN nanocomposites with a thickness of 1, 2, 3, 4, and 5 mm to evaluate the results from the changes of the thickness. As shown in Figure 8b, when the thickness is 1 mm, there is almost no absorption observed in the range of 1−18 GHz; however, the other maximum absorption peaks all reached below −20.0 dB at different thicknesses covered with the band range of 1−18 GHz, which ensures the practical application of the full-wave band absorption materials by adjusting the thickness of the device.

The possible mechanism of the enhanced microwave absorption could be explained by the comparison of the complex relative permittivity and permeability of GN, α-Co nanocrystals, β-Co nanospheres, and their GN nanocomposites with a thickness of 2 mm. It is obvious in Figure 9 that for GN the values of the real and imaginary parts of the permittivity are very high, with permittivity decreases as the frequency increases (Figure 9a,b), but the value of the real and imaginary parts of the permeability vary a lot with frequency increases (Figure 9c,d). This result indicates the excellent conductivity of the GN sample and the lack of magnetic property, which may be the cause of its unsatisfying performance for microwave absorption. For α-Co nanocrystals and β-Co nanospheres, the values of the real and imaginary parts of the permittivity are very low, but the values of the real and imaginary parts of the permeability are relatively stable with frequency increases. This result indicates the relatively weak dielectric properties and the excellent hysteresis performance of the Co samples, which contribute to the magnetic loss for microwave absorption. To obtain an improved EM-absorption property, it is necessary for a microwave absorbent to possess an excellent dielectric loss aroused by suitable permittivity. However, for the impedance match, too high of a permittivity is disadvantageous and will result in strong reflection and weak absorption. Therefore, a low real part of the permittivity and an appropriately high electrical conductivity are favorable for microwave-absorbing materials.[58−61] For the two Co/GN nanocomposites (Figure 9a−d), α-Co/GN has a lower real part of the permittivity, an appropriate electrical conductivity, and a more appropriate conductivity for the dielectric loss as well as a more stable permeability for magnetic loss than the β-Co/Co nanocomposites, which are responsible for their improved microwave-absorbing performance. Thus, we conclude that a perfect match of the permittivity (a higher dielectric loss) and permeability (a stable magnetic loss) at an appropriate thickness of the microwave-absorbing materials is favorable for the improvement of their microwave absorption.

4. CONCLUSIONS

We have demonstrated an effective and versatile strategy for synthetizing α-Co nanocrystals and β-Co nanospheres grown on GN nanosheets, leading to the protection and dispersion of Co nanostructures through GN networks. As a microwave-absorbing material for use in effective shielding devices, the α-Co nanocrystals/GN nanocomposites exhibits excellent electromagnetic performance, which can be ascribed to the excellent electrical properties of the GN nanosheets, the small size and the phase of the Co nanostructures, and the electromagnetic match in the microstructures. The method presented in this work is very useful for enhancing the microwave-absorption properties of these electromagnetic materials with high RL at the full-wave band of 1−18 GHz, which expands the potential application range of magnetic metal nanomaterials used in microwave-absorbing areas.

■ ASSOCIATED CONTENT

Ⓢ Supporting Information

SEM image of β-Co/GN nanocomposites. This material is available free of charge via the Internet at http://pubs.acs.org.

■ AUTHOR INFORMATION

Corresponding Authors

*E-mail: mashulan@bnu.edu.cn (S.M.).
*E-mail: gbsun@bnu.edu.cn (G.S.).

Author Contributions

All authors have given approval to the final version of the manuscript.

Notes

The authors declare no competing financial interest.

■ ACKNOWLEDGMENTS

This work was supported by the Natural Science Foundation of China (NSFC; nos. 21271001, 21271028, and 51272030)

■ REFERENCES

(1) Bregar, V. B. *IEEE Trans. Magn.* **2004**, *40*, 1679−1684.

(2) Snoek, J. L. *Physica* **1948**, *14*, 207−217.

(3) Gambardella, P.; Rusponi, S.; Veronese, M.; Dhesi, S. S.; Grazioli, C.; Dallmeyer, A.; Cabria, I.; Zeller, R.; Dederichs, P. H.; Kern, K.; Carbone, C.; Brune1, H. *Science* **2003**, *300*, 1130−1133.

(4) Zhang, D. F.; Zhang, Q.; Huang, W. F.; Guo, L.; Chen, W. M.; Chu, W. S.; Chen, C. P.; Wu, Z. Y. *ACS Appl. Mater. Interfaces* **2012**, *4*, 5643−5649.

(5) Li, N.; Hu, C. W.; Cao, M. H. *Phys. Chem. Chem. Phys.* **2013**, *15*, 7685−7689.

(6) Han, Z.; Li, D.; Wang, H.; Liu, X. G.; Li, J.; Geng, D. Y.; Zhang, Z. D. *Appl. Phys. Lett.* **2009**, *95*, 023114-1−023114-3.

(7) Li, J. L.; Yi, X.; Ye, H. T. *Carbon* **2010**, *48*, 4574−4577.

(8) Sun, Z. K.; Sun, B.; Qiao, M. H.; Wei, J.; Yue, Q.; Wang, C.; Deng, Y. H.; Kaliaguine, S.; Zhao, D. Y. *J. Am. Chem. Soc.* **2012**, *134*, 17653−17660.

(9) Baaziz, W.; Begin-Colin, S.; Pichon, B. P.; Florea, I.; Ersen, O.; Zafeiratos, S.; Barbosa, R.; Begin, D.; Pham-Huu, C. *Chem. Mater.* **2012**, *24*, 1549−1551.

(10) Baranauskas, V. V.; Zalich, M. A.; Saunders, M.; Pierre, T. G. S.; Riffle, J. S. *Chem. Mater.* **2005**, *17*, 5246−5254.

(11) Zhou, Z. H.; Liu, G. J.; Han, D. H. *ACS Nano* **2009**, *3*, 165−172.

(12) Schällibaum, J.; Torre, F. H. D.; Caseri, W. R.; Löffler, J. F. *Nanoscale* **2009**, *1*, 374−381.

(13) Zadoina, L.; Soulantica, K.; Ferrere, S.; Lonetti, B.; Respaud, M.; Mingotaud, A. F.; Falqui, A.; Genovese, A.; Chaudret, B.; Mauzaca, M. *J. Mater. Chem.* **2011**, *21*, 6988−6994.

(14) Metwalli, E.; Korstgens, V.; Schlage, K.; Meier, R.; Kaune, G.; Buffet, A.; Couet, S.; Roth, S. V.; Rohlsberger, R.; Muller-Buschbaum, P. *Langmuir* **2013**, *29*, 6331−6340.

(15) Zalich, M. A.; Vadala, M. L.; Riffle, J. S.; Saunders, M.; Pierre, T. G. S. *Chem. Mater.* **2007**, *19*, 6597−6604.

(16) Barea, E.; Batlle, X.; Bourges, P.; Corma, A.; Fornés, V.; Labarta, A.; Puntes, V. F. *J. Am. Chem. Soc.* **2005**, *127*, 18026−18030.

(17) Bragança, L.; Avillez, R.; Moreira, C.; Pais da Silva, M. *Mater. Chem. Phys.* **2013**, *138*, 17−28.

(18) Wang, H.; Cui, L.; Yang, Y.; Casalongue, H.; Robinson, J.; Liang, Y.; Cui, Y.; Dai, H. *J. Am. Chem. Soc.* **2010**, *132*, 13978−13980.

(19) Xue, D. J.; Xin, S.; Yan, Y.; Jiang, K. C.; Yin, Y. X.; Guo, Y. G.; Wan, L. J. *J. Am. Chem. Soc.* **2012**, *134*, 2512−2515.

(20) Novoselov, K.; Geim, A.; Morozov, S.; Jiang, D.; Zhang, Y.; Dubonos, S.; Grigorieva, I.; Firsov, A. *Science* **2004**, *306*, 666−669.

(21) Li, Y.; Wang, H.; Xie, L.; Liang, Y.; Hong, G.; Dai, H. *J. Am. Chem. Soc.* **2011**, *133*, 7296−7299.

(22) Chandra, V.; Park, J.; Chun, Y.; Lee, J.; Hwang, I.; Kim, K. *ACS Nano* **2010**, *4*, 3979−3986.

(23) Liang, J.; Xu, Y.; Sui, D.; Zhang, L.; Huang, Y.; Ma, Y.; Li, F.; Chen, Y. *J. Phys. Chem. C* **2010**, *114*, 17465−17471.

(24) He, H.; Gao, C. *ACS Appl. Mater. Interfaces* **2010**, *2*, 3201−3210.

(25) Shen, J.; Hu, Y.; Shi, M.; Li, N.; Ma, H.; Ye, M. *J. Phys. Chem. C* **2010**, *114*, 1498−1503.

(26) Zhou, G.; Wang, D.; Li, F.; Zhang, L.; Li, N.; Wu, Z.; Wen, L.; Lu, G.; Cheng, H. *Chem. Mater.* **2010**, *22*, 5306−5313.

(27) Su, J.; Cao, M. H.; Ren, L.; Hu, C. W. *J. Phys. Chem. C* **2011**, *115*, 14469−14477.

(28) Guo, S.; Sun, S. *J. Am. Chem. Soc.* **2012**, *134*, 2492−2495.

(29) Wang, H.; Casalongue, H.; Liang, Y.; Dai, H. *J. Am. Chem. Soc.* **2010**, *132*, 7472−7477.

(30) Chen, Y.; Wang, Q.; Zhu, C.; Gao, P.; Ouyang, Q.; Wang, T.; Ma, Y.; Sun, C. *J. Mater. Chem.* **2012**, *22*, 5924−5927.

(31) He, F.; Niu, N.; Qu, F.; Wei, S.; Chen, Y.; Gai, S.; Gao, P.; Wang, Y.; Yang, P. *Nanoscale* **2013**, *5*, 8507−8516.

(32) Yang, S.; Gao, P.; Bao, D.; Chen, Y.; Wang, L.; Yang, P.; Li, G.; Sun, Y. *J. Mater. Chem. A* **2013**, *1*, 6731−6735.

(33) Ji, Z.; Shena, X.; Song, Y.; Zhu, G. *Mater. Sci. Eng., B* **2011**, *176*, 711−715.

(34) Lin, S.; Yu, J.; Wang, F.; Wei, Y.; Yuan, B.; Zhu, H. *Funct. Mater. Lett.* **2013**, *06*, 1350042.

(35) Sato, H.; Kitakami, O.; Sakurai, T.; Shimada, Y.; Otani, Y.; Fukamichi, K. *J. Appl. Phys.* **1997**, *81*, 1858−1862.

(36) Puntes, V. F.; Zanchet, D.; Erdonmez, C. K.; Alivisatos, A. P. *J. Am. Chem. Soc.* **2002**, *124*, 12874−12880.

(37) Diana, F. S.; Lee, S. H.; Petroff, P. M.; Kramer, E. J. *Nano Lett.* **2003**, *3*, 891−894.

(38) Grass, R. N.; Stark, W. J. *J. Mater. Chem.* **2006**, *16*, 1825−1830.

(39) Nam, K. M.; Shim, J. H.; Ki, H.; Choi, S. I.; Lee, G.; Jang, J. K.; Jo, Y.; Jung, M. H.; Song, H.; Park, J. T. *Angew. Chem., Int. Ed.* **2008**, *47*, 9504−9508.

(40) Puntes, V. F.; Zanchet, D.; Erdonmez, C. K.; Alivisatos, A. P. *J. Am. Chem. Soc.* **2002**, *124*, 12874−12880.

(41) Dinega, D. P.; Bawendi, M. G. *Angew. Chem., Int. Ed.* **1999**, *38*, 1788−1791.

(42) Sun, S.; Murray, C. *J. Appl. Phys.* **1999**, *85*, 4325−4330.

(43) Zhou, Z.; Liu, G.; Han, D. *ACS Nano* **2009**, *3*, 165−172.

(44) Bao, Y.; An, W.; Turner, C. H.; Krishnan, K. M. *Langmuir* **2010**, *26*, 478−483.

(45) He, Q. L.; Yuan, T. T.; Luo, Z. P.; Haldolaarachchige, N.; Young, D. P.; Wei, S. Y.; Guo, Z. H. *Chem. Commun.* **2013**, *49*, 2679−2681.

(46) Chen, T. T.; Deng, F.; Zhu, J.; Chen, C. F.; Sun, G. B.; Ma, S. L.; Yang, X. J. *J. Mater. Chem.* **2012**, *22*, 15190−15197.

(47) Nethravathi, C.; Rajamathi, M. *Carbon* **2008**, *46*, 1994−1998.

(48) Ibrahim, M.; Marcelot-Garcia, C.; Atmane, K.; Berrichi, E.; Lacroix, L.; Zwick, A.; Warot-Fonrose, B.; Lachaize, S.; Decorse, P.; Piquemal, J.; Viau, G. *J. Phys. Chem. C* **2013**, *117*, 15808−15816.

(49) Matsumoto, M.; Miyata, Y. *IEEE Trans. Magn.* **1997**, *33*, 4459−4464.

(50) Singh, P.; Babbar, V.; Razdan, A.; Puri, R.; Goel, T. *J. Appl. Phys.* **2000**, *87*, 4362−4366.

(51) Maeda, T.; Sugimoto, S.; Kagotani, T.; Tezuka, N.; Inomata, K. *J. Magn. Magn. Mater.* **2004**, *281*, 195−205.

(52) Sun, G. B.; Dong, B. X.; Cao, M. H.; Wei, B. Q.; Hu, C. W. *Chem. Mater.* **2011**, *23*, 1587−1593.

(53) Sun, G. B.; Zhang, X. Q.; Cao, M. H.; Wei, B. Q.; Hu, C. W. *J. Phys. Chem. C* **2009**, *113*, 6948−6954.

(54) Wen, H.; Cao, M. H.; Sun, G. B.; Xu, W. G.; Wang, D.; Zhang, X. Q.; Hu, C. W. *J. Phys. Chem. C* **2008**, *112*, 15948−15955.

(55) Wang, T.; Liu, Z.; Lu, M.; Wen, B.; Ouyang, Q.; Chen, Y.; Zhu, C.; Gao, P.; Li, C.; Cao, M.; Qi, L. *J. Appl. Phys.* **2013**, *113*, 024314-1−024314-8.

(56) Sun, X.; He, J.; Li, G.; Tang, J.; Wang, T.; Guo, Y.; Xue, H. *J. Mater. Chem. C* **2013**, *1*, 765−777.

(57) Kong, L.; Yin, X.; Zhang, Y.; Yuan, X.; Li, Q.; Ye, F.; Cheng, L.; Zhang, L. *J. Phys. Chem. C* **2013**, *117*, 19701−19711.

(58) Huynen, I.; Quievy, N.; Bailly, C.; Bollen, P.; Detrembleur, C.; Eggermont, S.; Molenberg, I.; Thomassin, J. M.; Urbanczyk, L.; Pardoen, T. *Acta Mater.* **2011**, *59*, 3255−3266.

(59) Bollen, P.; Quievy, N.; Huynen, I.; Bailly, C.; Detrembleur, C.; Thomassine, J. M.; Pardoena, T. *Scr. Mater.* **2013**, *68*, 50−54.

(60) Kong, L.; Yin, X.; Ye, F.; Li, Q.; Zhang, L.; Cheng, L. *J. Phys. Chem. C* **2013**, *117*, 2135−2146.

(61) Kong, L.; Yin, X.; Kong, L.; Yin, X.; Zhang, L.; Cheng, L. *J. Am. Ceram. Soc.* **2012**, *95*, 3158−3165.